THEORY OF NEAR FIELD OPTICS

Christian Girard
Laboratoire de Physique Moléculaire UA CNRS 772
Université de Franche-Comté
25030 Besançon Cedex, FRANCE .

Alain Dereux
Institute for Studies in Interface Sciences, FUNDP
61, Rue de Bruxelles, 5000 NAMUR,
BELGIUM .

Olivier J. F. Martin
Swiss Federal Institute of Technology, ETH-Zentrum
CH-8092 Zurich
SWITZERLAND .

Abstract. *The optical imaging of micro- and nanometric objects requires the detection of non-radiative field components confined at the vicinity of their surface. Since 1984, numerous experimental applications of this concept in Near Field Optics (NFO) have been demonstrated and a broad variety of Scanning Near Field Optical Microscopes (SNOM) have been elaborated and continuously improved. In order to guide the ongoing developments of this new subwavelength optical probing method, as well as to refine the understanding of the contrast mechanisms involved in NFO, several theoretical frameworks have already been proposed and considerable modelling work has been performed. The present paper will be devoted to a detailed analysis of the NFO image formation mechanisms of three-dimensional (3D) objects. In order to circumvent the obstacles inherent to the matching of the electromagnetic boundary conditions on the surface of complex objects, this analysis will be presented in the framework of the Integral Equation Formalism (IEF). Two original numerical schemes, both based on a different discretization procedure, will be discussed; and several numerical applications on systems of experimental interest will be presented. Particularly, the problem of near field distributions around 3D-objects of various sizes and shapes will be discussed as a function of experimental parameters.*

1 Introduction

Some fifteen years ago, the first optical topographic signals with subwavelength resolutions, were recorded independently by different groups in the world [1]. In fact, these pionnering works were encouraged and stimulated by intriguing theories and speculations about the strange properties of evanescent and confined fields concentrated near the surface of materials [2-5]. Since this exploratory period, a broad variety of Scanning Near Field Optical Microscopes (SNOM) have been elaborated and continuously improved [6-18]. Simultanously, in order to guide the ongoing developments of this new subwavelength

O. Marti and R. Möller (eds.), Photons and Local Probes, 1–20.

optical probing method as well as to get more insights on the contrast mechanisms involved in near field optics (NFO), numereous theoretical frameworks were developed and considerable modelling works were performed [19-37]. Actually, this new local probe technique was challenging regarding the limited number of predictive theoretical schemes devoted to optical phenomena associated with mesoscopic structures. Van Labeke and Barchiesi recently reviewed the various theoretical methods [31]. Among the recent published works, one already may distinguish different trends.

First, as extensively discussed in refs.[24,25,31], the perturbative diffraction method provides an interesting framework to study low relief objects. In this case the boundary conditions problem is solved by assuming that the fluctuation heights of the surface are weak compared to the incident wavelength. Corrections to the usual result associated with a perfectly flat sample are obtained in terms of the Fourier tranform of the corrugation function limiting the surface of the solid. This method represents an interesting tool towards the interpretation of SNOM images and does not need extensive computational work. Nevertheless, we have to emphasize that such a perturbative approximation limit its validity range to surface corrugations of weak amplitude [38].

The complex problem related to the field distribution calculations inside SNOM devices [27] can also be investigated with theories based on diffraction gratings [39-41]. Such an approach is interesting because gratings are quite often used in SNOM. The different vector theories of diffraction gratings were reviewed in a paper by Maystre [40]. Within this scheme, the periodicity of the two interacting systems (sample plus probe), requires to describe the detection process by introducing an artifial periodic array of identical tips supported by a flat surface [31]. Similar periodic arrays of metallic nano-protrusions were also introduced in some early STM current calculations [42,43]. In these two examples, the periodic structure is necessary to make feasible the application of the scattering theory. In NFO the artificial coupling between the tips can be avoided by increasing the period of the spatial array.

The propagation of light through nanometer-sized structures can also be investigated by applying powerful numerical methods based on localized mutipolar distributions. For example the Multiple-Multi-Pole (MMP) technique developed by Hafner [44], turns out to be well suited to study many theoretical aspects related to NFO (radiation pattern, gap width dependence, imaging properties, ...). The main idea of MMP is to introduce fictive multipolar distributions along the boundaries of the different domains in which the field is calculated. Some two years ago, this method was applied to two-dimensional aperture SNOM by Novotny and Pohl [34,35] and more details about this approach can be found in the paper by Novotny in these proceedings [45].

Other theoretical analysis of NFO mechanisms (ultimate resolution, image-object relation, ...) have been proposed [28,29,30]. So recently, the important issue concerning the inverse scattering reconstruction problem in NFO has been adressed by Garcia and Nieto-Vesperinas [30]. This analysis was developed within the range of validity of the Rayleigh hypothesis. See for instance the papers of Garcia and Nieto-Vesperinas in these proceedings [46].

It is also possible to overcome the difficulties inherent to the low symmetry of SNOM devices by solving directly the integral equation associated with Maxwell's equations [20-22,32,33,36,37,47-49]. The kernel of the master equation can then be factorized into two different ways leading to two different kinds of dyadic propagators: ***Green functions*** or

Field-susceptibilities. This technique associated with a convenient discretization procedure has proven to be powerful and versatile for studying SNOM [20,21,22,36,37]. The statements of this real space approach will be reviewed in the following section (2). Numerical applications on systems of experimental interest will then be discussed in the other sections.

2) Field distribution around three-dimensional objects

As already mentioned in the introduction, Maxwell's equations are traditionally solved by matching the electromagnetic boundary conditions at the scatterers interfaces. On the other hand, general solutions of Maxwell's equations, for both arbitrary geometries and materials parameters can also be obtained using the integral equations formalism (IEF). This approach has been extensively discussed in a recent series of papers [20-22,36,37]. This section will be devoted to the application of a such real space approache to the computation of the field distributions lying around three-dimensional objects deposited on a surface, as a function of usual experimental parameters (object size, incident polarization, incident beam direction, ...).

2-1) Vector Lippmann-Schwinger equation for 3D-objects

In the present subsection, we outline the analytical framework for our numerical simulations. The principle of our method relies on the splitting into two parts of the physical system for which we are seeking a solution of the vectorial wave equation: a highly symmetrical reference system (in the simulations to be discussed below, the perfect planar surface limiting the infinite homogeneous half-spaces (cf. Fig. 1), and a perturbation embedded in this reference system (for example the 3D-defect lying on the perfect surface). By perturbation we do not mean that its physical properties differ slightly from the reference system, but rather that the perturbation is spatially limited within the reference system [21,22,36,37].

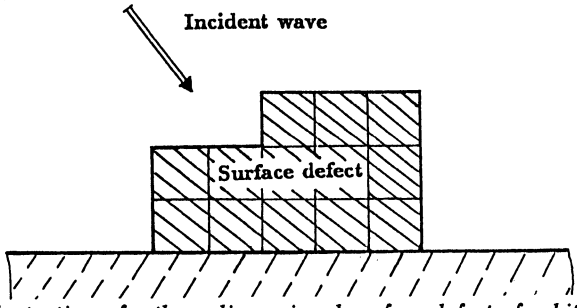

Fig.1: Schematic illustration of a three-dimensional surface defect of arbitrary shape lying on a flat surface (the reference system). The whole system is submitted to an incident optical excitation.

Let $\mathbf{E}_0(\mathbf{r},\omega)$ be the known Fourier component of the incident field on the highly symmetrical system. In the presence of the perturbation (3D-localized surface defect) the perturbed field $\mathbf{E}(\mathbf{r},\omega)$ obeys the following implicit Lippmann-Schwinger equation (L.S.) [50]

$$\mathbf{E}(\mathbf{r},\omega) = \mathbf{E}_0(\mathbf{r},\omega) + \int \mathbf{K}(\mathbf{r},\mathbf{r}',\omega).\mathbf{E}(\mathbf{r}',\omega)d\mathbf{r}' \qquad (1)$$

In this self-consistent equation, the dyadic kernel $\mathbf{K}(\mathbf{r},\mathbf{r}',\omega)$ may be factorized into two

equivalent ways depending on the adopted point of view.

(i)When working in the framework of the Field-Susceptibility Method (FSM), this factorization reads [20,36,37,51]

$$\mathbf{K}(\mathbf{r},\mathbf{r}',\omega) = \mathbf{S}(\mathbf{r},\mathbf{r}',\omega).\chi(\mathbf{r}',\omega) \tag{2}$$

where $\mathbf{S}(\mathbf{r},\mathbf{r}',\omega)$ represents the field susceptibility of the reference system [51] (cf. Figure (1)) and $\chi(\mathbf{r}',\omega)$ is the linear susceptibility of the perturbation (localized defect). In the case of ***continuous matter***, $\chi(\mathbf{r}',\omega)$ is given in terms of the local dielectric constant $\epsilon(\omega)$ associated with the surface defect (CGS units)

$$\chi(\mathbf{r}',\omega) = \frac{\epsilon(\omega) - 1}{4\pi} \tag{3}$$

for all the points $\mathbf{r}'$ located inside the surface defect, and

$$\chi(\mathbf{r}',\omega) = 0 \tag{4}$$

outside the perturbation. This factorization was originally introduced to we deal with atoms or molecules adsorbed on a surface [52,19,20]. Indeed, if one considers, for example, a system formed of p individual molecules, $\chi(\mathbf{r},\omega)$ can be expressed as [37]

$$\chi(\mathbf{r}',\omega) = \sum_{i=1}^{p} \alpha^{(i)}(\omega)\delta(\mathbf{r}' - \mathbf{r}_i) + ... \tag{5}$$

where $\mathbf{r}_i$ represents the position vectors of the molecules and $\alpha^{(i)}(\omega)$ defines their optical dipolar polarizabilities.

(ii) The second point of view is based on the following factorization [21,22,53] of the kernel $\mathbf{K}(\mathbf{r},\mathbf{r}',\omega)$

$$\mathbf{K}(\mathbf{r},\mathbf{r}',\omega) = \mathbf{G}(\mathbf{r},\mathbf{r}',\omega).\mathbf{V}(\mathbf{r}',\omega) \tag{6}$$

Where $\mathbf{G}(\mathbf{r},\mathbf{r}',\omega)$ is the Green's dyadic of the reference system and $\mathbf{V}(\mathbf{r}',\omega)$ is the dyadic defined by

$$\mathbf{V}(\mathbf{r}',\omega) = -\frac{\omega^2}{c^2}\frac{\epsilon(\omega) - 1}{4\pi} \tag{7}$$

for all points $\mathbf{r}'$ located inside the surface defect, and

$$\mathbf{V}(\mathbf{r}',\omega) = 0 \tag{8}$$

outside the perturbation. This factorization is standard in classical electrodynamics works. It emphasizes that the IEF formalism is aimed at treating discrete as well as continuous perturbations. Therefore the transition from classical to quantum electrodynamical problems can be performed in a single framework. Comparison of equations (2) and (6) indicates that the only difference between $\mathbf{S}(\mathbf{r},\mathbf{r}',\omega)$ and $\mathbf{G}(\mathbf{r},\mathbf{r}',\omega)$ is a dimensional factor.

2-2) Discretization procedures

An essential strength of both descriptions is the spatial localization of the surface defects which allows to solve exactly the self-consistent equation (1). In the present paper, two original numerical schemes, both based on a different discretization procedure will be

discussed and several numerical applications on systems of experimental interest will be presented.

(i) DIRECT RESOLUTION OF L.S. EQUATION

By using the factorization (2),the 3D-discretization of L.S. equation leads to [20-22]

$$\mathbf{E}(\mathbf{r},\omega) = \mathbf{E}_0(\mathbf{r},\omega) + \frac{(\epsilon(\omega)-1)}{4\pi}\sum_{k=1}^{n} W_k \mathbf{S}(\mathbf{r},\mathbf{R_k},\omega)\cdot\mathbf{E}(\mathbf{R_k},\omega), \tag{9}$$

where W_k represents the volume of the k^{th} discretized element and n is the total number of elements. Note that the discretization of the surface defect can be viewed as a numerical procedure to take mesoscopic objects of arbitrary shape into account. The set of vectors $\{\mathbf{E}(\mathbf{R_k},\omega)\}$ can be determined by standard linear algebra procedure. Thus by setting $\mathbf{r} = \mathbf{R_i}$ in equation (9), one obtains the following matrix equation to be solved numerically:

$$\mathcal{F}(\omega) = \mathcal{A}(\omega) \bullet \mathcal{F}_0(\omega), \tag{10}$$

where the symbol $\bullet$ indicates a total contraction on both Cartesian indexes and positions of discretized elements. Moreover $\mathcal{F}(\omega)$ and $\mathcal{F}_0(\omega)$ are two supervectors defined by

$$\mathcal{F}(\omega) = \{\mathbf{E}(\mathbf{R_1},\omega);\mathbf{E}(\mathbf{R_2},\omega);.....;\mathbf{E}(\mathbf{R_n},\omega)\} \tag{11}$$

and

$$\mathcal{F}_0(\omega) = \{\mathbf{E}_0(\mathbf{R_1},\omega);\mathbf{E}_0(\mathbf{R_2},\omega);.....;\mathbf{E}_0(\mathbf{R_n},\omega)\} \tag{12}$$

In Eq. (10), the (3n x 3n) matrix $\mathcal{A}$ is built from the different components of the field susceptibility $\mathbf{S}$ for all the possible $\{\mathbf{R_i},\mathbf{R_k}\}$ couples

$$\mathcal{A}(\omega) = [\mathbf{I} - \frac{(\epsilon(\omega)-1)}{4\pi}\mathcal{B}(\omega)]^{-1} \quad , \tag{13}$$

where $\mathbf{I}$ represents the identity tensor, and $\mathcal{B}(\omega)$ is the (3n x 3n) matrix defined by

$$\mathcal{B}(\omega) = \begin{pmatrix} W_1\mathbf{S}(\mathbf{R_1},\mathbf{R_1},\omega) & W_1\mathbf{S}(\mathbf{R_1},\mathbf{R_2},\omega) & ..... & W_1\mathbf{S}(\mathbf{R_1},\mathbf{R_n},\omega) \\ W_2\mathbf{S}(\mathbf{R_2},\mathbf{R_1},\omega) & W_2\mathbf{S}(\mathbf{R_2},\mathbf{R_2},\omega) & ..... & W_2\mathbf{S}(\mathbf{R_2},\mathbf{R_n},\omega) \\ ..... & ..... & ..... & ..... \\ ..... & ..... & ..... & ..... \\ W_n\mathbf{S}(\mathbf{R_n},\mathbf{R_1},\omega) & W_n\mathbf{S}(\mathbf{R_n},\mathbf{R_2},\omega) & ..... & W_n\mathbf{S}(\mathbf{R_n},\mathbf{R_n},\omega) \end{pmatrix} \tag{14}$$

This matrix contains all the dynamical and structural information on the interaction of the surface defect with the reference system. The diagonal terms describe the direct coupling between each discretized element and the substrate; whereas the off-diagonal terms are responsible for the interactions between these elements. Note that, when the number n remains finite, the self-consistent equation (10) can be solved exactly to obtain the amplitudes of the effective fields $\mathbf{E}(\mathbf{R_k},\omega)$. Furthermore when the size of the dynamical square matrix $\mathcal{A}(\omega)$ remains reasonable ($n \leq 500$), it is possible to derive accurate numerical solutions for the effective field distribution contained in the supervector $\mathcal{F}(\omega)$. Let us recall that in the present description the surface defect is assumed to be homogeneous and isotropic. Nevertheless, there is no difficulty to include anisotropic effects.

The above-described discretization procedure has also a physical meaning if we adopt a microscopic point of view and consider the matter as a set of discrete polarizable entities. In that case, the linear susceptibilities $\chi(\mathbf{R_k},\omega)$ are accounting for the electromagnetic response of each individual microscopic piece of matter. The density of the discretization grid is then related to the size of the elementary physical components that can be excited by the incident electromagnetic field $\mathbf{E_0}$. These excitable entities are scattering the incoming field and the electromagnetic near-field results from their self-consistent interactions. This point of view evidences the possible inclusion of quantum susceptibilities, non-linearities and transient effects in our computational framework. It opens a possible way to the theoretical study of SNOM imaging of individual molecules adsorbed on surfaces. This is of importance in view of the expected molecular resolution in NFO [18]. This computational scheme can also be extended to the study of localized plasmon resonnances occurring near metallic aggregates deposited on a flat surface. The study of such resonnances requires electronic non-local effects to be taken into account. As described in ref.[37], this can be realized by introducing appropriate non-local susceptibilitites in the self-consistent equation.

(ii) RESOLUTION BASED ON THE PARALLEL USE OF L.S. AND DYSON EQUATION

Instead of solving L.S. equation directly, is it also possible to apply an original and robust iterative scheme that allows to handle accurately very large dynamical matrices [33,48,49]. This section outlines the algorithmic features of this procedure. Another paper by the authors inside these proceedings details the physical content of this algorithm [53].

Once again, the 3D-surface defect is divided into n discretization meshes. The two matrix equations arising from the simultaneous discretization in direct space of both L.S. and Dyson's equations can be expressed by using the factorization (2)

$$\mathbf{E}(\mathbf{R_i},\omega) = \mathbf{E_0}(\mathbf{R_i},\omega) + \frac{(\epsilon(\omega)-1)}{4\pi}\sum_{k=1}^{n} W_k \mathbf{S}(\mathbf{R_i},\mathbf{R_k},\omega)\cdot\mathbf{E}(\mathbf{r_j},\omega), \qquad (15)$$

and

$$\mathcal{S}(\mathbf{R_i},\mathbf{R_j},\omega) = \mathbf{S}(\mathbf{R_i},\mathbf{R_j},\omega) + \frac{(\epsilon(\omega)-1)}{4\pi}\sum_{k=1}^{n} W_k \mathbf{S}(\mathbf{R_i},\mathbf{R_k},\omega)\cdot\mathcal{S}(\mathbf{R_k},\mathbf{R_k},\omega) \qquad (16)$$

where $\mathcal{S}(\mathbf{r},\mathbf{r}',\omega)$ represents the field-susceptibility of the whole system (reference system + surface defect). In fact, Dyson's equation is can be considered as a generalisation of L.S. equation for propagators.

These two equations may be solved simultaneously from the zero-order solutions $\mathbf{E_0}(\mathbf{r},\omega)$ and $\mathbf{S}(\mathbf{r},\mathbf{r}',\omega)$ associated with the reference system, by increasing the perturbation domain mesh by mesh from zero to its final size. The detailed procedure starts with the computation of the field distribution and the corresponding propagator resulting from the introduction of the first perturbation mesh $k = 1$ above the reference system (cf. Fig.2). The resulting system of equations is solved in two steps. First we apply the self-consistent equations arising when $i = 1$ in order to extract the field inside the discretization mesh $k = 1$. The field and the new propagator are then generated outside the first mesh by applying once again both L.S. and Dyson's equations. In the second step, this procedure is repeated for the next perturbation meshe; and so as, until all the meshes of the perturbation domain have been taken into account. This second discretization scheme provides

a convenient basis for handling large scale optical systems, such as those used in NFO. Moreover, by reducing the self-consistent problem to a succession of small matrix (3×3) inversions (cf. Fig.2), this iterative scheme is relevant for all the studies concerned with a great number of degrees of freedom.

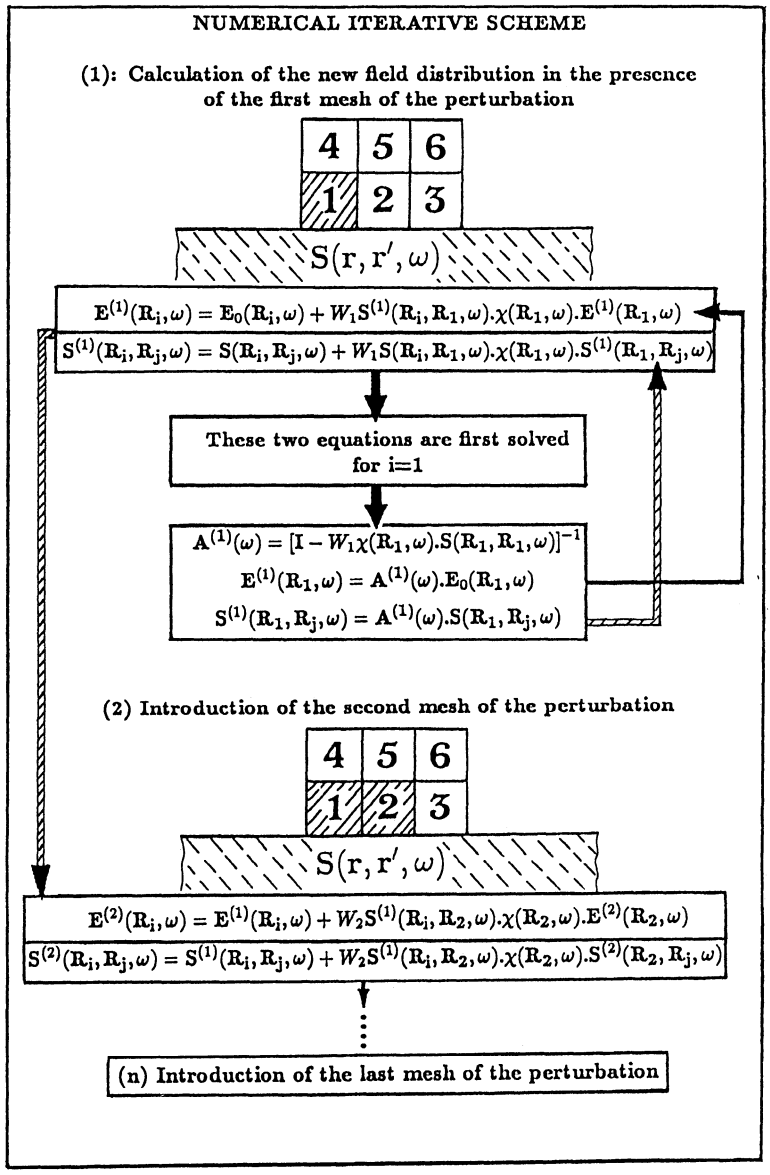

Fig.2: *Diagrammatic representation of a numerical scheme based on the parallel resolution of both Lippmann-Schwinger and Dyson's equation. The two first steps of the numerical sequence are sketched.*

2-3) Numerical applications

Our first example considers a 3D-localized defect of parallelepipedic shape lying on a perfectly flat surface (cf. Fig.3). The reference system is the flat surface for which the propagator $\mathbf{S}(\mathbf{r},\mathbf{r}',\omega)$ may be found in the literature [51]:

$$\mathbf{S}(\mathbf{r},\mathbf{r}',\omega) = \mathbf{S_0}(\mathbf{r},\mathbf{r}',\omega) + \mathbf{S_s}(\mathbf{r},\mathbf{r}',\omega) \tag{17}$$

where $\mathbf{S_0}(\mathbf{r},\mathbf{r}',\omega)$ is the so-called retarded propagator in vacuum and $\mathbf{S_s}(\mathbf{r},\mathbf{r}',\omega)$ describes the correction to $\mathbf{S_0}(\mathbf{r},\mathbf{r}',\omega)$ due to the presence of the surface. The retarded propagator $\mathbf{S_0}(\mathbf{r},\mathbf{r}',\omega)$ in vacuum has a simple analytical form that only depends on the difference $\mathbf{R} = \mathbf{r} - \mathbf{r}'$ [51]:

$$\mathbf{S_0}(\mathbf{r},\mathbf{r}',\omega) = exp(-i\frac{\omega}{c}\mathbf{R})\{-\frac{\omega^2}{c^2}\mathbf{T_1}(\mathbf{R}) + i\frac{\omega}{c}\mathbf{T_2}(\mathbf{R}) + \mathbf{T_3}(\mathbf{R})\} \tag{18}$$

with

$$\mathbf{T_1}(\mathbf{R}) = \frac{\mathbf{RR} - \mathbf{I}R^2}{R^3} \tag{19}$$

and

$$\mathbf{T}_\gamma(\mathbf{R}) = \frac{3\mathbf{RR} - \mathbf{I}R^2}{R^{\gamma+2}} \tag{20}$$

where $\mathbf{I}$ represents the unit dyadic and the index $\gamma = 2$ or 3.

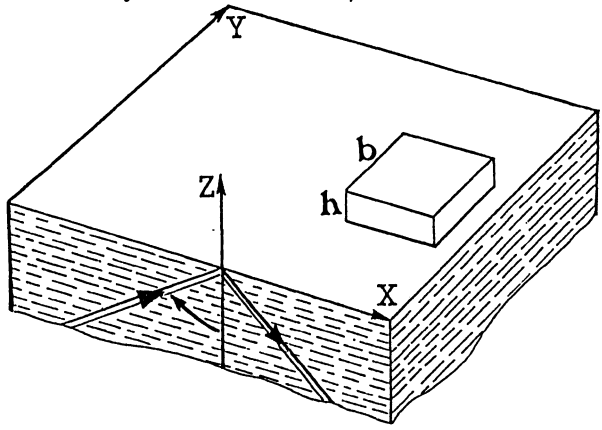

Fig.3: *Perspective representation of a square shaped mesoscopic surface defect lying on a flat surface. The system is illuminated in total reflection and the incident wavelength in vacuum is equal to 620 nm. The object is 100 nm high and the side of its square section b = 500 nm.*

Figure 4 displays the behaviour of the normalized field intensity defined by

$$I = \frac{|E|^2}{|E_0|^2} \tag{21}$$

In this ratio, E represents the amplitude of the self-consistent field, and E_0 the amplitude of the incident field (i.e. in the absence of the surface defect). The calculation of I is

performed in an observation plane parallel to the reference system, placed at a distance $z_0 = 25$ nm above the square shaped surface defect. This observation plane, is introduced merely for the convenience of data visualization, since the field can be computed for any arbitraty position inside the system by using equation (9). In the internal reflection setup described in Figure 3, the zeroth order solution $\mathbf{E_0}(\mathbf{r},\omega)$ is the evanescent field created by total reflection at the surface $Z = 0$ [12-17,54]. Such an illumination configuration introduced in near field optical microscopy by Ferrell *et al*, Courjon *et al* and Van Hulst and collaborators [12-14], eliminates propagating waves along the z-direction. .

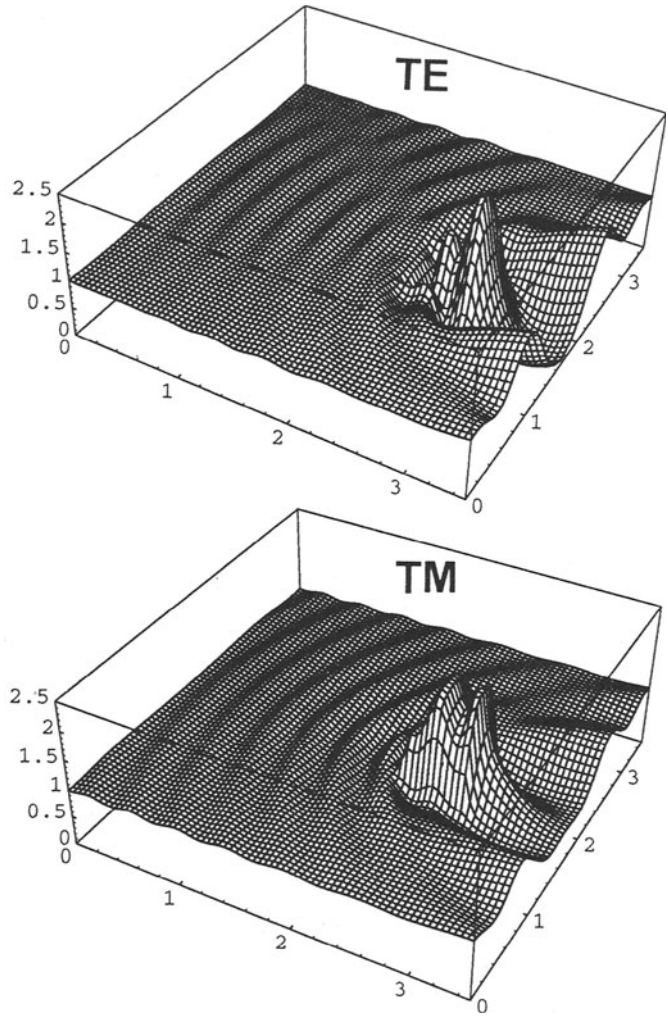

Fig.4: *3D-perspective view of the normalized electric field intensity* $I = \frac{|E|^2}{|E_0|^2}$ *calculated above the scattering system schematized in Figure 3. The two principal TM and TE polarization modes are investigated for a same propagation direction, and the length scales are expressed in microns.*

It may be seen on Figure 4, that the two large scale (3500×3500) nm^2 calculated images are very complex. They display a complicated standing field pattern currently observed in the STOM/PSTM configurations, namely, strong confined field effects observed just above the scatter, scattering along its lateral sides and usual interference patterns due to the interaction between the travelling surface wave and the surface wave reflected by the defect. When the number of defects per unit area increases, this interference pattern issued from the multiple scattering is the surface plane will give rise to the phenomenon called "speckle pattern". In particular, these 3D-perspective views indicate that at about 25 nm from the top of the object, the enhancement factor of the field intensity reaches 2.5. We also note that the fringe amplitudes which, of course, depends on the size of the scatterer are sensitive to the polarization of the field. As described in the recent experimental works of Van Hulst *et al* [55], generally for larger objects the interference phenomenon dominates and makes the detection of subwavelength features difficult.

What we have so far proved with this introductive simulation is that, first the 3D-objects confine the electromagnetic field around them and second that the relation between the object profile and the resulting spatial field distribution may be very complex. Actually, this finding forces us to address a fundamental question in NFO: what would be both optimal lighting configuration and optimal object dimension for which the field distribution would tend to closely reproduce to the object profile. In order to answer this important problem we consider the low symmetry system described in Figure 5.

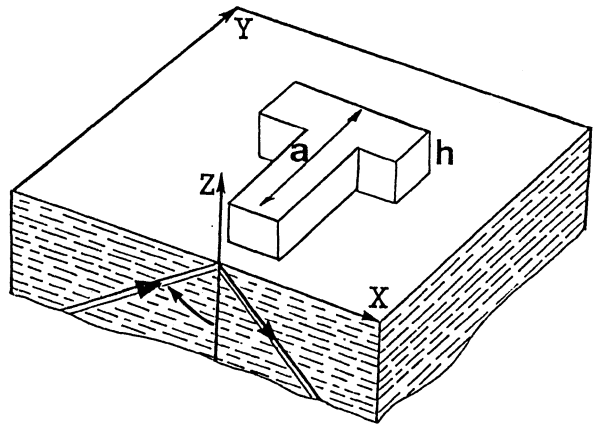

a=720nm, h=90nm a	a=480nm, h=60nm b
a=240nm, h=30nm c	a=80 nm, h=10nm d

Fig.5: *Schematic illustration of a T-shaped surface defect lying on a flat surface illuminated in internal total reflection. For the same incident wavelength, four sizes, defined by a and h, will be successively investigated.*

In order to get more insights on the behaviour of the ***field pattern-object profile relation***, we study in Figures 6 and 7 the evolution of the contour plots image upon reduction of the T-shaped protrusion. The two usual polarisation modes TE and TM are considered in Figures 6 and 7. Four different typical sizes have been successively investigated. In the first example (Figure 6-a) we start in the mesoscopic range (the letter is 720 nm long and 90 nm high). In the three other examples, a reduction factor equal to 1.5, 3 and 9 is successively applied, and the position of the observation plane is reduced in the same proportion.

In a first step we consider the TE polarization (cf. Figure 6).

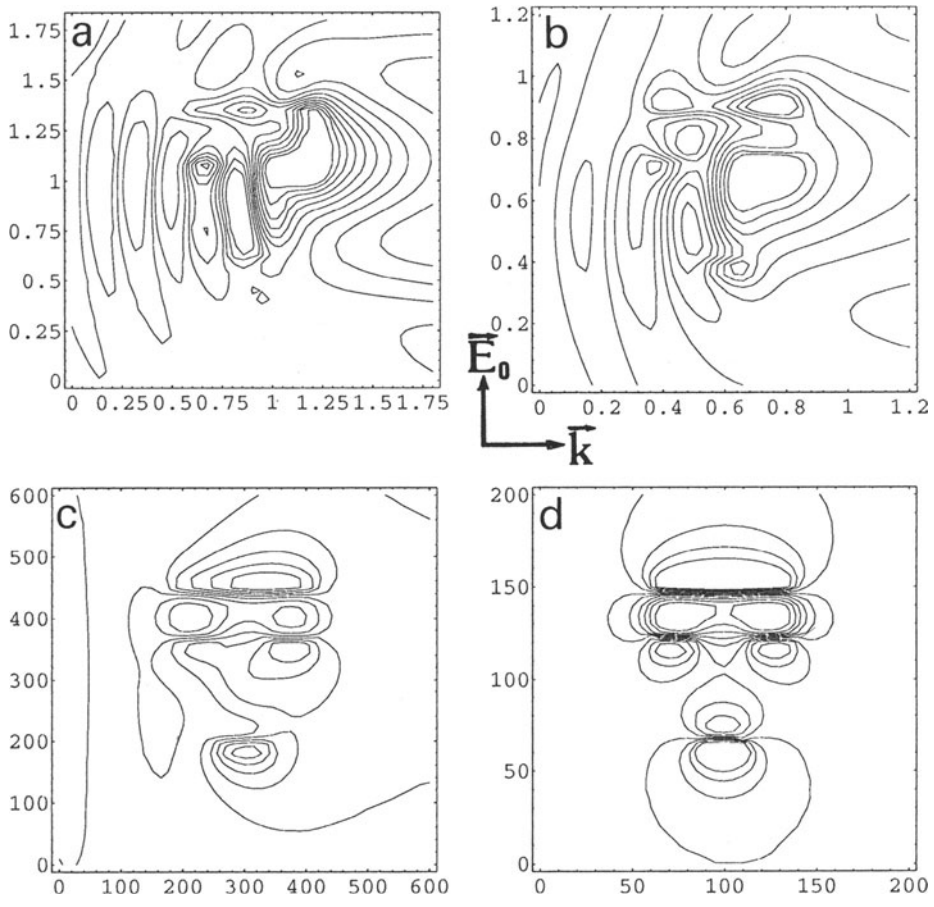

Fig.6: *A sequence of electric field intensity contour plots calculated in the TE polarization; the corresponding sizes of the object are given in figure 5 and* **k** *represents the wave vector of the surface wave; (a and b): the axes are labelled in microns; (c and d): the axes are labelled in nanometers.*

Some comments may be done about the evolution of the field pattern.

(i) First, when the object displays mesoscopic dimensions (see Figs. 6-a and 6-b),

the field distribution outside and inside the T-shaped protrusion is dominated by interference phenomena so that the field contour plots do not follow the profile of the T-shaped protrusion.

(ii) Second, as the dimensions of the 3D-object enter the subwavelength range (cf. Figs. 6-c and 6-d), the interference pattern around the object progressively collapses and the field distribution tends to become perfectly symmetrical thereby reproducing the symmetry of the letter **T**. Under such conditions, a highly localized field occurs just above the edges located in a perpendicular direction to the incident field E_0.

In fact, when we deal with such subwavelength sized objects, the importance of retardation effects decreases dramatically, so that the symmetry of the field distribution is only governed by both the orientation of the incident field and the profile of the object itself. Actually, these features may help us to get more insights into this complex contrast phenomenon. The field distribution is now governed by the depolarization effect which results in the conservation of the normal component of the induction vector $\mathbf{D}(\omega) = \epsilon(\omega)\mathbf{E}(\omega)$ upon crossing the surfaces of the T-shaped protrusion. Due to the strong variation of the dielectric constant between air and glass, this statement imposes a sharp variation of the field near the interfaces perpendicular to E_0.

We now turn to the TM polarization case described below.

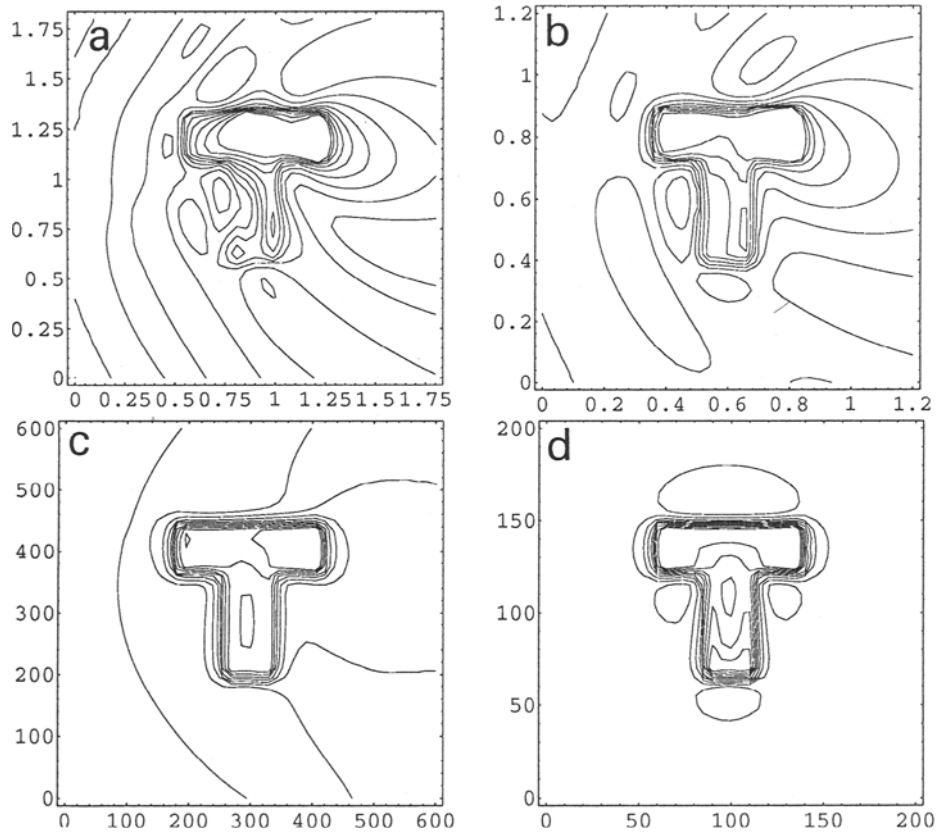

Fig.7: *Same that Figure 6 but in TM mode*

In this mode the polarization of the surface wave is mainly dominated by Z component of the incident field. The main resulting effect is, as expected, a better image-object relation. One can observes that, when the size of the T-shaped protrusion is gradually reduced, the field distribution around the object tends to perfectly reproduce its profile.

3 Image reconstruction

In SNOM devices the use of a pointed detector allows the convertion of the non-radiative fields concentrated near the surface irregularities into radiative fields detectable in the far-field region. The amount of optical energy converted by such devices depends mainly on the shape and on the size of the region of interaction with the confined fields described in Figures 6 and 7. It is also very sensitive to both the object parameters and the illumination conditions (internal total reflection, angle of illumination, external illumination, ...).

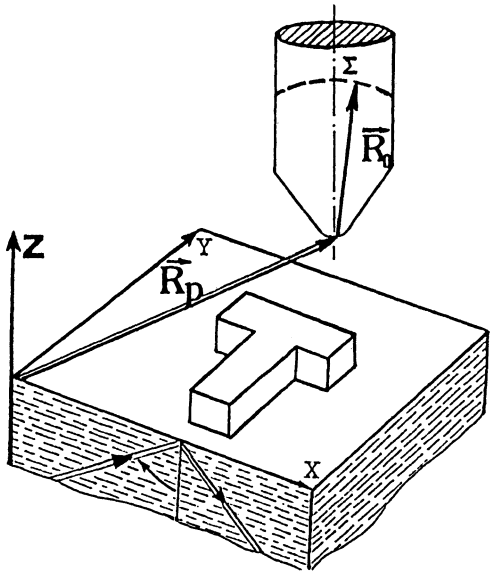

Fig.8: *Schematic illustration of a scanning probe device working in the STOM/PSTM configuration. The vector* $\mathbf{R}_D = (X, Y, Z)$ *defines the detector apex position and* $\mathbf{R}_0$ *characterizes the location of the wave zone* Σ *inside the detector.*

The tip-sample coupling can be included in our formalism without no formal difficulty. This can be done merely by adding a second perturbation in the self-consistent scheme described in previous sections (2-2) and (2-3). In particular, the discretization procedure already used for taking into account the 3D-object can be extended to the tip-apex of the detector. The conversion mechanism will then be analysed theoretically using the theory described above. In fact, the knowledge of the effective field distribution inside the perturbation (tip-apex + surface defect) is sufficient to describe the far-field $\mathbf{E}_{far}$ crossing a surface Σ located inside the wave zone of the dielectric stylus (cf Fig.(8)). From equation

(9) we can write

$$\mathbf{E_{far}}(\mathbf{R_0}+\mathbf{R_p},\omega)=\mathbf{E}_0(\mathbf{R_0}+\mathbf{R_p},\omega)+\mathcal{E}_{pr}(\mathbf{R_0}+\mathbf{R_p},\omega)+\mathcal{E}_{ob}(\mathbf{R_0}+\mathbf{R_p},\omega) \quad (22)$$

with

$$\mathcal{E}_{ob}(\mathbf{R_0}+\mathbf{R_p},\omega)=\frac{(\epsilon(\omega)-1)}{4\pi}\sum_{k=1}^{n}W_k\mathbf{S}(\mathbf{R_0}+\mathbf{R_p},\mathbf{R_k},\omega)\cdot\mathbf{E}(\mathbf{R_k},\omega) \quad (23)$$

and

$$\mathcal{E}_{pr}(\mathbf{R_0}+\mathbf{R_p},\omega)=\frac{(\epsilon_{pr}(\omega)-1)}{4\pi}\sum_{k=n+1}^{n+m}W_k\mathbf{S}(\mathbf{R_0}+\mathbf{R_p},\mathbf{R_k},\omega)\cdot\mathbf{E}(\mathbf{R_k},\omega) \quad (24)$$

where $\mathbf{R_p}$ defines the location of the tip apex with respect to an absolute reference frame, the vector $\mathbf{R_0}$ represents the position of a point of the Σ surface with respect to the apex of the detector [37] and $\epsilon_{pr}(\omega)$ is the optical dielectric constant of the detector. By using an asymptotic form for the the propagator $\mathbf{S}$ in the far field range, it is possible to describe regions far away from the perturbation. Finally, numerical integration of the Poynting vector associated with $\mathbf{E}_{far}(\mathbf{R_p}+\mathbf{R_0},\omega)$ on the surface of the cross section Σ of the probe leads to the energy flux across that section and hence to the detected intensity $I(\mathbf{R_p},\omega)$ that is the relevant observable in experiments.

3-1) Scanning over subwavelength 3D-objects

The relations (22), (23) and (24) defined in the previous sections are general since they account for the real profile of both the tip-apex and the object. From these equations it is possible to calculate the signal $I(\mathbf{R_p},\omega)$ and to simulate, by scanning the detector, **SNOM** images. Both quasi-point and spatially extended probe tips will be considered in our calculations.

(i) IMAGING WITH QUASI-POINT PROBE TIPS

Our first example considers the problem of near field image calculations of a three-dimensional dielectric subwavelength object lying on a perfectly flat glass surface (the reference system). In order to minimize the tip sample coupling we have considered, in a first step, a quasi-point tip apex (2.5 nm curvature at its extremity and 10 nm height). The three-dimensional object used in this first application is a letter **F** of optical index 1.5, thickness 7.5 nm and height 35 nm. Once again, we considered the internal total reflection (**STOM/PSTM**) configuration described in refs.[12-17,54], with an incident wavelength λ =632 nm. For the computation, we formed a Cartesian discretization grid consisting of three consecutive layers of 76 cubic elements of size 2.5 nm.

Figure 9 displays a sequence of gray scale images of this object calculated at constant distance from the reference system. In these images the object induces a strong field confinement for both TM and TE polarizations. In the TM mode, the defect induces a well-localized increase of the near-field distribution directly related to the shape of the object. According to the results of the previous sections, the image-object relation of subwavelength structures appears to be optimal when the incident electric field is perpendicular to the interface plane. A different feature occurs in the TE image where the incident field polarization is parallel to the surface of the reference system. In this case, some spatial region located above the object appears in reversed contrast relative to the object relief. The spatial extension of the contrast reversal regions is determined

by the size of the localized surface corrugation. Moreover, in the direction parallel to the incident beam, an enhanced confinement is found above the edges of the object. Such an electromagnetic confinement could explain the high resolution obtain by D. Courjon and *coworkers* when working in TE mode while recording low relief objects [56](5nm in thickness).

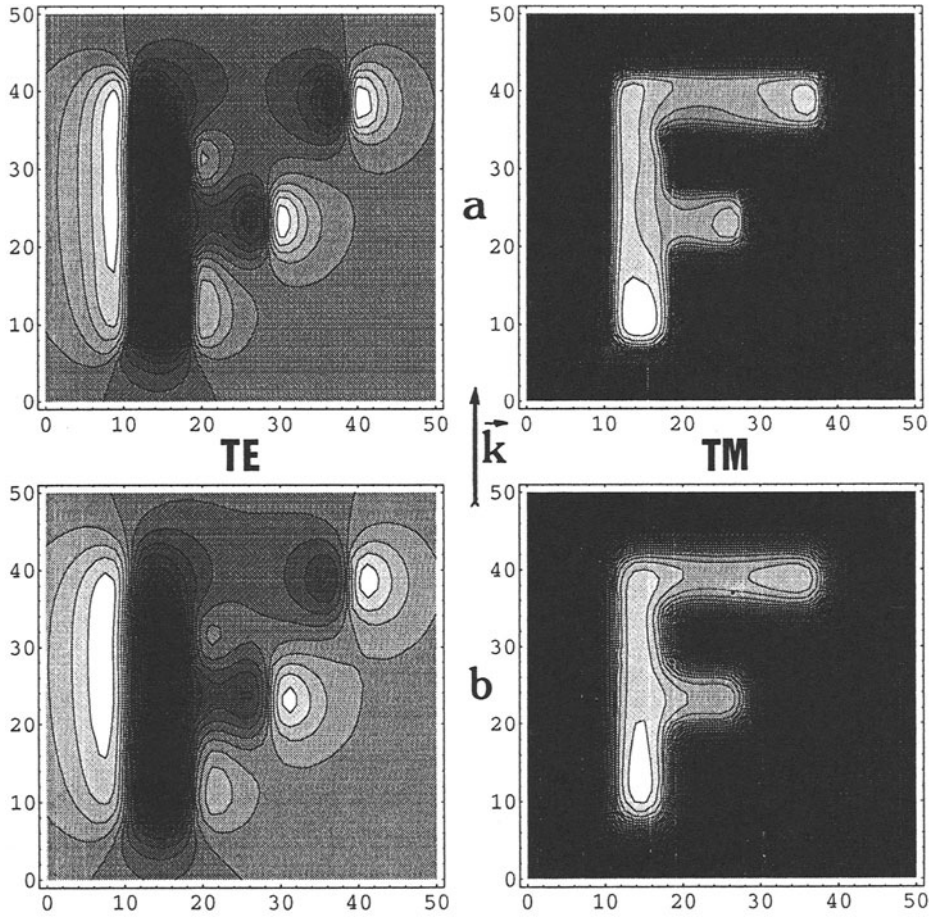

Fig.9: *A sequence of grey scale images of* **F** *shaped surface protrusion of 7.5 nm in thickness and 35 nm in height. The evolution of the image is given as a function of the approach distance for two different external polarization (transvers electric and transvers magnetic). The incident wave vector is parallel to the OY axis (black arrow on the Figures). The intensity* $I(\mathbf{R_p})$ *collected by the probe was calculated in a plane parallel to the reference system at a distance Z from the plane surface. The scanned area is* (50×50) nm^2 *and the incident wavelength is 632 nm. This simulation was performed with a quasi-punctual tip apex (2.5 nm curvature at its extremity and 10 nm height).*

a: $Z = 10$ *nm;* **b**: $Z = 15$ *nm.*

The phenomenon of reversal contrast can be simply explained by examining the sign of the dominating short-range term $\mathbf{T_3}(\mathbf{r_0},\mathbf{r_a})$ composing the free space propagator $\mathbf{S_0}$ (cf. Eq. 20 and ref.[20]). In fact when a small element of the very tip (located at $\mathbf{r_0}$) passes over an element of the surface defect (located at $\mathbf{r_a}$), $\mathbf{T_3}(\mathbf{r_0},\mathbf{r_a})$ takes the form, with $\mathbf{r_0}-\mathbf{r_a}=(0,0,z_0-z_a)$:

$$\mathbf{T_3}(\mathbf{r_0},\mathbf{r_a}) = \begin{pmatrix} -[z_0-z_a]^{-3} & 0 & 0 \\ 0 & -[z_0-z_a]^{-3} & 0 \\ 0 & 0 & 2[z_0-z_a]^{-3} \end{pmatrix} \tag{25}$$

The near-field generated inside the very tip deduced from Eq.(9) can then be approximated by

$$\mathbf{E}(\mathbf{r_0},\omega) \simeq \mathbf{E_0}(\mathbf{r_0},\omega) + W_k \frac{\epsilon(\omega)-1)}{4\pi} \mathbf{T_3}(\mathbf{r_0},\mathbf{r_a},\omega).\mathbf{E}(\mathbf{r_a},\omega). \tag{26}$$

As a consequence of the minus sign in the first row of Eq.(25), the second term of Eq.(26) appears in phase opposition to the evanescent field in the TE mode

$$\mathbf{E_0}(\mathbf{r_0},\omega) = (E_0(\mathbf{r_0},\omega),0,0), \tag{27}$$

which results in a near-field decrease in the immediate proximity of the sample. In the TM mode, the z-component dominates and imposes a positive sign on $\mathbf{T_3}$. Note that a similar behaviour has been observed in the framework of the diffraction theory described in ref. [57]. This contrast reversal may appear more familiar when considering depolarisation effects. In the TE mode, the incident electric field is oriented along the y direction, so that the finite size of the object induces strong depolarization effects which reduce the intensity of the electric field inside the object. In the TM mode, the incident electric field has a large vertical component (along z) and a tiny horizontal component (along x) which interact with each other inside the object. As indicated by equation (25), the z-component dominates at short distances, so that scanning in a detection plane above the object is more sensitive to the vertical depolarization which masks the horizontal depolarization effect.

(ii) IMAGING WITH EXTENDED PROBE TIPS

In a practical STOM/PSTM configuration, the pointed fiber is brought near the sample in a region where the magnitude of the evanescent field is intense. The evanescent illumination reduces the amount of stray light entering the taper laterally, so that the part of the detector which is located outside the decay range of the surface near-field contributes weakly to multiple scattering effects between the tip and the sample. A fairly good approximation then allows us to limit the height of the pointed fiber to the decay length η of the evanescent field. η reaches about 100 nm if the evanescent field is generated by a plane wave which is incident slightly above the critical angle of total reflection. In the analysis of the imaging process with extended probe tips, we therefore restricted the height of the conical probe tip to 100 nm. The tip apex had a realistic curvature radius of 15 nm. This truncated detector was then discretized on a Cartesian grid by stacking layers of meshes in a closed packed arrangement. The detector described above was brought above a T-shaped three-dimensional object engraved on a transparent glass sustrate. This T was 5 nm thick and 70 nm long. Many of the features found in the case of a quasi-point detector are recovered. In particular, depolarization effects follow

the same trends as observed for a quasi-point probe. From our simulations we conclude that the sharp resolution of the object is still possible with an extended detector. The loss of quality related to the growing size of the detector may be appreciated by comparing Figures (9a) and (9b) with Figures (10a) and (10b).

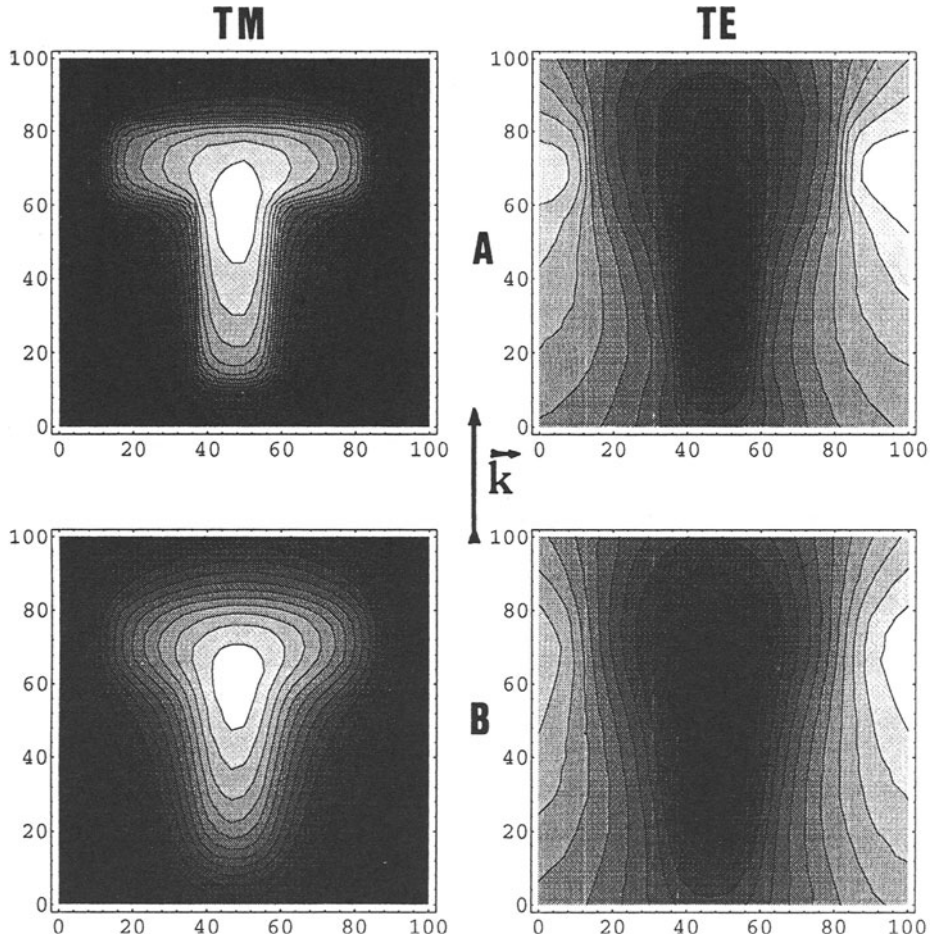

Fig.10: *Simulated images of a letter* **T** *engraved on a transparent substrate of optical index of refraction 1.5. The thickness and the height of this 3D pattern are 5 nm and 70 nm respectivily. The calculation was performed with a probe tip of realistic size discretized with 54 cells positionned in a closed packed arrangement (15 nm curvature at its extremity, 100 nm nanometer height). The vector* $\mathbf{k}_0$ *represents the projection of the incident wave vector on the plane (XOY). Two different approach distances were considered:*

a: *Z =6 nm;* **b:** *Z =10 nm.*

For an approach height of 10 nm, the quasi-point probe tip provides a sharper image

than the extended tip. But the extended probe tip can recover a sharp image by coming 5 nm closer to the sample.

We tested the stability of the image profile versus the number of layers used to discretize the conical tip. Increasing the number of layers from 5 to 7 did not affect the lateral variation of the detected intensity, but contributed to the signal background. In other words, extending the tip further changed the absolute value of the intensity but not the relative definition of the image. This emphasizes the fact that the confined field responsible for the observed image is set up by the objects themselves. How to couple the near-field associated to the objects with the radiative far-field is the basic question related to the tip design, that is important to achieve a convenient detection level while reducing the noise.

4 Conclusion

We have presented some numerical applications relevant to the principles and the technology of near-field optical microscopy. Our direct space approach is based on a general theoretical framework that handles the self-consistent electromagnetic field arising from scattering by three-dimensional objects and gives access to observables that are relevant experimentally, such as the light intensity collected by a NFO probing system (an STOM/PSTM tip for example). We have used this model to investigate the imaging properties in a STOM/PSTM configuration, of subwavelength three-dimensional objects lying on a surface. Our results show that a strong confinement of the electromagnetic field in the vicinity of these three-dimensional objects is responsible for the extraordinary resolution observed experimentally. The topography of this confined field, and therefore the collected image, depend strongly on the polarization of the evanescent field used for illuminating the object. When the electric field is parallel to the surface supporting the object (TE field), a strong field confinement arises along the object interfaces orthogonal to the field and the image-object relation emphasizes the outline of the object; different orientations of the incident field highlight different sides of the object. When a TM field is used, the field pattern reproduces the shape of the object. In this situation, the image emphasizes the entire volume of the object and is independent of the orientation of the incident field. This explains the high sensitivity of experimental images to the operating polarization. The influence of the detector geometry and of the probing distance on image formation has also been considered. In particular we have shown that the coupling between the apex of the detector and the object plays a principal role in the imaging process: beyond a given detector size, the image remains unchanged. We found that the loss of resolution associated with an extended tip may be counterbalanced by approaching the tip closer to the sample. This property could orientate near field optical instrumentation to improve tip-sample control in order to optimize the detection of the confined field set up by the objects themselves.

Acknowledgments:

This work was performed in the framework of the Human Capital and Mobility Programm *"Near-field Optics for Nanoscale Science and Technology"* initiated by the European Community. The authors have benefitted of useful discussions with D. Courjon, D. W. Pohl, O. Marti, L. Novotny, U. Fischer, M. Spajer and N. Van Hulst.

References

[1] For an historical presentation of Near-Field Optics, see for example D. W. Pohl in "Near Field Optics" **NATO series E**, Edited by D. W. Pohl and D. Courjon,(Kluwer, Dordrecht, (1993)) pp. 1-5.

[2] E.H. Singe, Phil. Mag. **6**,356(1928).

[3] H.A. Bethe, Phys. Rev. **66**, 163(1944).

[4] E.A. Ash and Nichols, Nature,**237**,510(1972).

[5] U. Ch. Fischer and H.P. Zingsheim, J. Vac.Sci. Technol. **19**,881(1981).

[6] D.W. Pohl, W. Denk, M. Lanz, Appl. Phys. Lett. **44**,651(1994).

[7] A. Lewis, M. Isaacson, A. Harootunian and A. Muray, Ultramicroscopy **13**, 227(1984).

[8] U. Ch. Fischer, J. Vac. Sci. Technol. **B3**,386(1985).

[9] A. Harootunian, E. Betzig, M. Isaacson and A. Lewis, Appl. Phys. Lett. **49**, 674(1986).

[10] E. Betzig, J. K. Trautman, T. D. Harris, J. S. Weiner and R. L. Kostelak, Science **251**,1468(1991) and references therein.

[11] K. Lieberman and A. Lewis, Ultramicroscopy **42-44**,399(1991).

[12] R. Reddick, R. J. Warmack and T.J. Ferrell, Phys. Rev. B**39**,767(1989).

[13] D. Courjon, K. Sarayeddine and M. Spajer, Opt. Com. **71**,23(1989).

[14] N. F. Van Hulst, F. B. Segerink, F. Achten and B. Bolger Ultramicroscopy **42-44**,416(1992).

[15] T. L. Ferrell, S. L. Sharp and R. J. Warmack, Ultramicroscopy **42-44**,408(1991).

[16] F. de Fornel, L. Salomon, P. Adam, E. Bourillot, J. P. Goudonnet and M. Neviere, Ultramicroscopy **42-44**422(1992).

[17] M. Specht, J. D. Pedarnig, W. M. Heckl and T. W. Hansch, Phys. Rev. Lett. **68**,476(1992).

[18] E. Betzig and R. J. Chichester, Science **262**,1422(1993).

[19] B. Labani, C. Girard, D. Courjon and D. Van Labeke, J. Opt. Soc. Am. **7** 936 (1990).

[20] C. Girard and D. Courjon, Phys. Rev. **B42**,9340(1990).

[21] A. Dereux, "*Théorie de l'optique de champ proche*", PhD Thesis, Faculté Universitaire N. D. de la Paix, NAMUR, Belgium(1991).

[22] A. Dereux, J.P. Vigneron, Ph. Lambin and A.A. Lucas, Physica **B175**,65(1991).

[23] A. Roberts, J. Appl. Phys. **70**,4045(1991).

[24] D. Van Labeke and D. Barchiesi, J. Opt. Soc. Am., **A9**,732(1992).

[25] D. Barchiesi and D. Van Labeke, J. Mod. Optics, **40**1239(1993).

[26] S. Berntsen, E. Bozhevolnaya and S. Bozhevolnyi, J. Opt. Soc. Am., **A10**,878(1993).

[27] J.P. Goudonnet, L. Salomon, F. De Fornel, E. Bourillot, P. Adam, M. Nevière and P. Guérin, Scann. Prob. Proc. SPIE, **1639** 12(1992).

[28] J. M. Vigoureux and D. Courjon, Applied Optics **31**3170(1992).

[29] J. M. Vigoureux, F. Depasse and C. Girard, Applied Optics, **31** 3036(1992).

[30] N. Garcia and M. Nieto-Vesperinas, Optics Letters **24** 2090(1993).

[31] D. Van Labeke and D. Barchiesi, in "Near Field Optics" **NATO series E**, Edited by D. W. Pohl and D. Courjon (Kluwer, Dordrecht, 1993)), pp. 157-178.

[32] A. Dereux and D. W. Pohl, in "Near Field Optics" **NATO series E**, Edited by D. W. Pohl and D. Courjon (Kluwer, Dordrecht, 1993)), pp. 189-198.

[33] A. Castiaux, A. Dereux, J.P. Vigneron, C. Girard and O.J.F. Martin, Ultramicroscopy (in press).

[34] L. Novotny, D. W. Pohl and P. Regli, Ultramicroscopy (in press).

[35] L. Novotny, D. W. Pohl and P. Regli, J. Opt. Soc. Am., **11** 1768(1994).

[36] C. Girard, A. Dereux and O.J.F. Martin, Phys. Rev. **B49**, 13872(1994).

[37] C. Girard and A. Dereux, Phys. Rev. **B49** 11344(1994).

[38] T.S. Rahman and A.A. Maradudin, Phys. Rev. **B21**504(1980).

[39] R. Petit, Topics in current Physics,**22** (Springer, Berlin, 1980).

[40] D. Maystre, Progress in Optics **21**, E. Wolf, ed. (Elsevier, Amsterdam, 1984).

[41] J.E. Harvey, Am. J. Phys. **47**, 974(1979).

[42] N. Garcia, C. Ocal and F. Flores, Phys. Rev. Lett. **50**,2002(1983).

[43] E. Stoll, A. Baratoff, A. Selloni, P. Carnevali, J. Phys. C: Solid State Phys. **17** 3073(1984).

[44] Ch. Hafner, "The Generalized Multiple Multipole Technique for computational Electromagnetics" (Artech, Boston, Mass., 1990).

[45] L. Novotny, in these proceedings.

[46] N. Garcia and M. Nieto-Vesperinas, in these proceedings.

[47] F. Pincemin, A. Sentenac and J.J. Greffet, J. Opt. Soc. Am. **A11** 1117(1994).

[48] O.J.F. Martin, A. Dereux and C. Girard, J. Opt. Soc. Am. **A11**,pp. 1073(1994).

[49] O.J.F. Martin, Ph. D. Thesis (EPFL Lausanne 1993).

[50] E. N. Economou, ***"Green's Functions in Quantum Physics"***, 2d. ed., (Springer, Berlin 1983).

[51] C. Girard and X. Bouju, J. Chem. Phys. **95**,pp. 2056-2064(1991).

[52] C. Girard and L. Galatry, Surf. Science **154**, 254(1985).

[53] A. Dereux, C. Girard and O.J.F. Martin, in these proceedings.

[54] H. Bielefeldt, B. Hecht, S. Herminghaus, O. Marti and J. Mlynek, in "Near Field Optics" **NATO series E**, Edited by D. W. Pohl and D. Courjon (Kluwer, Dordrecht, 1993)), pp. 281-286.

[55] N. F. Van Hulst, F. B. Segering and B. Bolger, Opt. Com. **87**,pp. 212-218(1992).

[56] D. Courjon, C. Bainier and M. Spajer, J. Vac. Sci. Technol. **B10**, pp. 2436-2439(1992).

[57] D. Barchiesi,"Modélisation des microscopes optiques en champ proche STOM et SNOM. Optimisation et Spectroscopie; Thesis (Université de Besançon, France, 1993).